

Life and failure of oriented carbon nanotubes composite electrode for resistance spot welding

Zhong Zheng¹ , Jiafeng Tao¹, Xing Fang¹, Huan Xue¹

¹Hubei University of Technology, Department of Mechanical Engineering, 430068, Wuhan, Hubei, China.

e-mail: zhengzh215@163.com; tjf18717191324@163.com; 13007106056@163.com; stonemechanics@163.com

ABSTRACT

In view of the poor weldability of electrodes in resistance spot welding (RSW) of galvanized steel sheets, the life of oriented multi-walled carbon nanotubes reinforced Cu matrix composites (Cu@MWCNTs/Cu) electrodes was studied, in which Cu coated multi-walled carbon nanotubes (MWCNTs) are arranged along the flow direction of working electric/force. By analyzing the macro/microscopic morphology, microstructure, hardness, texture and composition of the failed composite electrodes and the commercially CuCrZr electrode, the mechanism of the weldability enhancement and failure of electrodes was discussed. The results show that the life of Cu@MWCNTs/Cu electrodes (2150 welds) is 3 times longer than that of CuCrZr electrode (600 welds), and the degradation rate is much slower. The hardness of Cu@MWCNTs/Cu electrodes is 30–40Hv higher. The content of recrystallized and recovery grains of Cu@MWCNTs/Cu electrodes is less. This is due to the pinning effect of MWCNTs, and straight and long MWCNTs are arranged along the electrical/force direction. These improve the hardness, mechanical properties, conductivity, and resistance to thermal deformation, cracking, and pitting of Cu@MWCNTs/Cu electrodes, which effectively slows down the failure rate and makes the spot welding life of Cu@MWCNTs/Cu electrodes longer. This work provides a new idea for the application of CNTs/Cu composites.

Keywords: Carbon Nanotube; Orientation Arrangement; Resistance Spot-Weld; Electrode; Failure.

1. INTRODUCTION

Galvanized steel sheet has the characteristics of high strength, corrosion resistance and low cost, so it is widely used in automobile body manufacturing. Each automobile body assembly generally requires 3500–6000 welds, more than 90% of which are carried out by resistance spot welding. The role of the electrodes is very important in the process of resistance spot welding. It transfers thousands of Newtons of force and tens of thousands of amperes of current to the workpieces, so that the resistance heat flow nugget is locally generated in the workpieces to weld, while more than 80% of the welding heat is exported. At present, CuCrZr, CrZr and other Cu alloy electrodes are widely used to weld galvanized steel plates in body factories. However, the weldability of galvanized steel is poor, and the surface zinc layer deteriorates the working environment of spot welding. A series of phenomena such as high temperature softening, tip plastic deformation (mushroom effect) of electrodes, formation of brittle layer of copper-zinc alloy, adhesion, pitting corrosion, wear, cracking and splashing occur, which lead to premature failure of electrodes.

In order to improve the service life and welding quality of resistance spot welding electrode in spot welding of galvanized steel sheets, many scholars have done a lot of research: (1) Strengthen the electrode surface. ERTEK EMRE and BOZKURT [1] used the electro-spark deposition (ESD) process to melt the Cr-Ni composite coating on the electrode surface. By increasing the hardness of the electrode tip, the electrode wear rate and softening rate were reduced, and the life of the electrodes when welding galvanized steel sheets was greatly improved. However, this method sacrifices part of the electric and thermal conductivity of the electrodes. In addition, due to the low deposition rate of ESD, and manual operation makes the composite coating thickness less stable, which limits its application in large-scale industrial production. MALMIR *et al.* [2] used the cathodic arc Physical Vapor Deposition (PVD) process to deposit a nano-multilayer CrN/(Cr,Al)N coating on the electrode surface, which enhanced the wettability, resistance to oxidation and thermal shock of the electrode tips, thereby slowing down the electrode failure rate. However, the coating is easy to fall off, and it also deteriorated the electrical and thermal conductivity of the electrodes. Therefore, this method has limited improvement in electrode life. (2) Design the special structure of the electrode tip. CHEN *et al.* [3] designed the electrode end

face as a central micro-concave, which effectively improved the connection strength of RSW joints. However, due to the concave and convex of the electrode end face, the depth of the welding welds indentation is inconsistent, and the welding quality is unstable. ZHAO *et al.* [4] designed centered annular on the end face of the ceramic composite electrodes, which can produce a larger nugget size of RSW joints, and reduce the indentation depth under the premise of ensuring the welding quality. But the electrode end face unevenness is difficult to control alignment so that welding stability is not high. LI *et al.* [5] designed the Newton ring on the electrode end face, which not only improved the RSW welding quality, but also delayed the wear of the electrodes and improved their life. However, this method still does not solve the problem that the upper and lower electrode rings are difficult to control alignment. (3) Strengthen electrode materials. WU *et al.* [6] first used deep cryogenic treatment to strengthen RSW electrodes materials and used it for resistance spot welding of galvanized steel sheets. The conductive and thermal conductivity of the cryogenic treated electrodes is obviously improved, but the hardness has no obvious change, and the RSW quality is still not stable enough.

In summary, the related research of RSW electrodes has not yet made substantial breakthroughs, and it is urgent to explore new ideas for the development of electrode materials. When the galvanized sheet is spot welded, the harsh working environment puts forward higher requirements for the electrode materials, that is, the mechanical properties, electrical/thermal conductivity and wear resistance should be superior. Our research group has designed and prepared MWCNTs/Cu composites for this requirement [7, 8]. We consider that the physical basis of the composite effect is derived from the difference in properties between the metal matrix and the reinforcements. In order to produce obvious benefits through enhancements, the performance of the reinforcements must far exceed the matrix. CNTs have nearly perfect bonding structure and many excellent properties [9]. Its axial theoretical thermal conductivity is as high as 2586–6000W/mK, which is ten times that of Cu electrode [10]. Its conductivity up to 10,000 times that of Cu [11]. It has good thermal stability, high temperature mechanical and excellent electrical properties. The aspect ratio of CNTs is extremely high, which is the key factor to determine the strength of the composites. In addition, the wear resistance of CNTs composites is excellent [12]. These make CNTs an ideal enhancements that can significantly improve the properties of the matrix, and do not damage its conductivity of the composites. In MWCNTs reinforced Cu matrix (Cu@MWCNTs/Cu) composites prepared by our group [7, 8], Cu-coated MWCNTs remain straight and long, and MWCNTs/Cu interface was tightly bonded. MWCNTs are uniformly dispersed in Cu matrix and arranged along the flow direction of working electric/force. The axial conductivity and thermal conductivity are 79.93%IACS and 376W/mK, respectively, achieving a balance between axial mechanical properties and conduction properties, which exactly meets the requirements of RSW electrode materials.

Therefore, we applied the above oriented Cu@MWCNTs/Cu composites to the RSW electrodes for galvanized steel sheets. The welding life of RSW electrodes was studied and compared with that of commercial CuCrZr electrode. The service life of Cu@MWCNTs/Cu electrode and CuCrZr electrode for spot welding of galvanized steel sheets was evaluated by combining the critical dimension of nugget and the tensile shear limit load (TSFL). The macro/microscopic morphology, microstructure, hardness, texture and composition of the failed electrodes were characterized by carbon imprinting, optical microscope, scanning electron microscopy (SEM), combined with X-ray diffraction (XRD) and electron backscatter diffraction (EBSD).

2. MATERIALS AND EXPERIMENTS

2.1. RSW electrodes

Cu@MWCNTs/Cu composite electrodes prepared by our group according to a series of processes such as chemical plating, powder mixing, sintering, hot extrusion, cold drawing and reverse extrusion [7, 8], as shown in Figure 1. In the prepared composite electrode, the MWCNTs coated with Cu remained straight and long, and the MWCNTs/Cu interface was tightly bonded. MWCNTs are uniformly dispersed in the Cu matrix and arranged along the direction of electrical/mechanical conduction during electrode operation, as shown in Figure 1(a). All these make MWCNTs have good axial conductivity and mechanical properties.

Cu@MWCNTs/Cu composite electrode was prepared by a series of processes such as electroless plating, powder mixing, sintering, hot extrusion, cold drawing and reverse extrusion [7, 8], as shown in Figure 1. In the prepared composite electrodes, Cu-coated MWCNTs remain straight and long, and MWCNTs/Cu interface is tightly bonded. MWCNTs are uniformly dispersed in Cu matrix and arranged along the flow direction of working electric/force during electrode operation, as shown in Figure 1(a) and Figure 2(a). All these make MWCNTs composite have good axial conductivity and mechanical properties.

Cu@MWCNTs/Cu electrode and CuCrZr electrode (commercially available) used in this work are $\phi 16 \times 23$ mm dome flat electrode of ASTM B169M-2005 standard. The characteristic data of the electrodes measured by experiments are shown in Table 1.

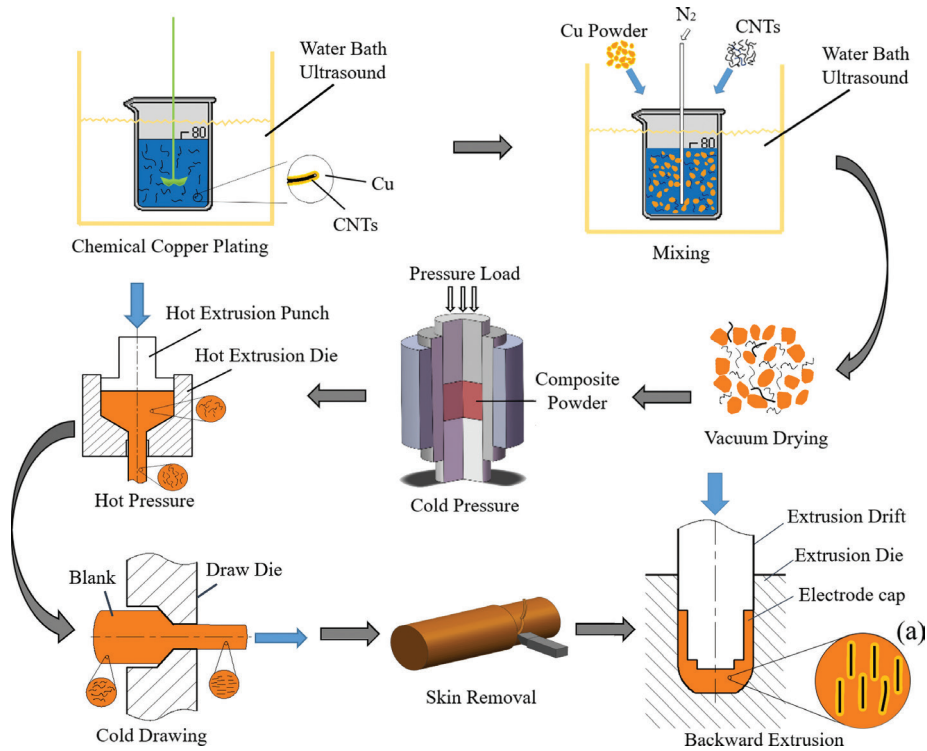


Figure 1: Manufacturing process of composite electrodes.

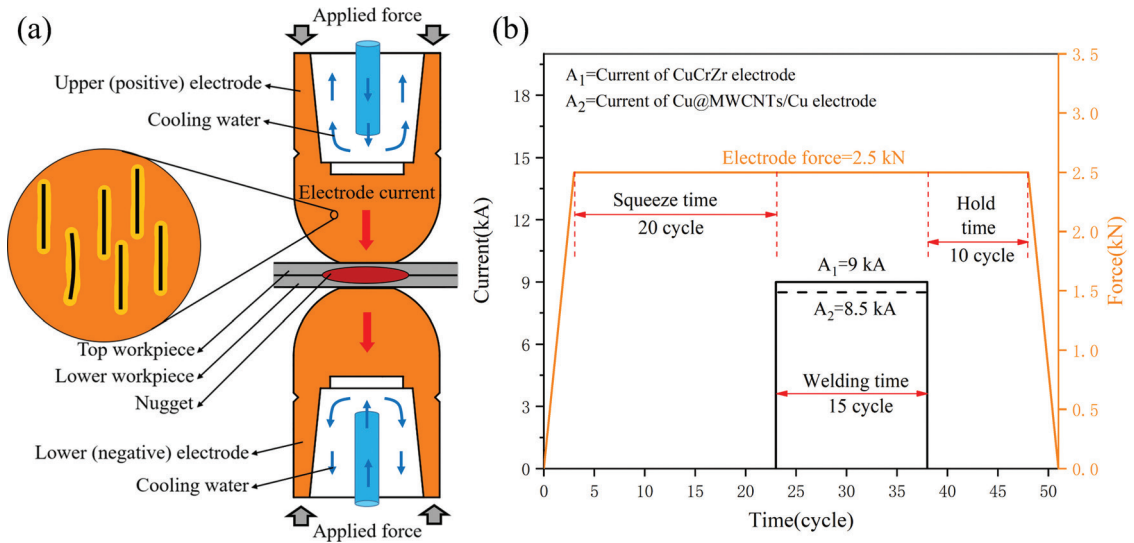


Figure 2: Test equipment and welding process: (a) RSW schematic diagram, (b) RSW process parameters.

Table 1: Characteristic data of the electrodes.

ELECTRODE	HARDNESS (HV0.1)	CONDUCTIVITY (%IACS)	THERMAL CONDUCTIVITY (W/mK)
Cu@MWCNTs/Cu	185	80.76	385
CuCrZr	145	75.25	330

Table 2: Chemical composition of DP600 dual phase steel (wt%).

C	M	Si	S	P	Al	N
0.1	1.4	0.15	0.008	0.07	0.02	0.009

2.2. Workpiece materials

The galvanized steel used here is DP600 galvanized dual phase steel, which has two specifications of $385 \times 60 \times 0.8\text{mm}$ and $100 \times 30 \times 0.8\text{mm}$, and the thickness of the galvanized layer is $10\mu\text{m}$. The chemical constituents are shown in Table 2.

2.3. Experimental method of RSW

The RSW experiments shown in Figure 2(a) were performed on a YR-350SA2HGE single-phase AC resistance spot welding machine. The resistance spot welding process determined by SYSWELD simulation and pre-experimental studies is shown in Figure 2(b). Before RSW, the surface of galvanized steel sheets is cleaned with anhydrous ethanol to remove dust and grease.

2.4. Test methods

In order to evaluate the life of electrodes, a set of nugget diameter measurement, nugget shear force detection and electrode tip diameter measurement were performed for every 100 welds during the RSW experiment, and the average value was taken as the nugget diameter and shear force of the $100 \times n$ (n is a positive integer) welds. The welding method on the small-sized galvanized steel sheets is shown in Figure 3(c), i.e., the 1–10 welds are welded at the lap joints of two small-sized galvanized steel sheets, and the 10 welds are used to measure and represent the diameter and shear resistance of the 1st welding nugget. Then, the welding is carried out on the large-sized galvanized steel sheets, as shown in Figure 3(a). After each welding of 90 welds, the last 10 welds are welded on the small-sized galvanized steel plate, and divided into 2 groups of 5 each. The two groups are welded according to the method shown in Figure 3(c), so as to prepare for the subsequent tearing test and shear tensile test. In order to ensure that the shear force acting on the spot welded joint during the shear tensile test is always consistent with the direction, a gasket of $30 \times 30 \times 0.8\text{mm}$ is placed at both ends of the galvanized steel sheet sample, as shown in Figure 3(d). The spot welding life of the electrodes is evaluated using the American Welding Association standard AWS/SAED8.9M:2002. The electrode life is the number of previous welds when the nugget diameter is less than $4\sqrt{\delta}$ (δ is the thickness of the welded workpiece, mm), or the number of previous welds when the shear strength of the weld is less than 80% of the shear strength of the 100th weld. Since the two methods have their own limitations, we use both methods to evaluate the electrode spot welding life.

In order to record the changes in surface shape and diameter of the upper and lower electrode tips during the resistance spot welding process, they were collected by means of carbon paper imprinting. A combination of white paper/carbon paper/white paper is placed on both sides of a steel plate, and the carbon paper impressions of the first, 100, 200, 300 ... welds are collected in sequence by applying electrode pressure without current. Then a camera is used to take pictures of the carbon imprinting on the white paper at the same focal length.

The composition and phase of the alloy layer at the end of the failed electrode were identified by X-ray diffractometer (Cu target, 2θ : $20\text{--}80^\circ$, scanning speed 5° per minute, scanning voltage 40kV , current 40mA). In order to characterize the metallographic and microstructure of the longitudinal section of the failed electrodes, the electrodes were longitudinally cut along the center line of the end face by wire electrical discharge machining. The longitudinal sections were characterized by an optical microscope (Nikon-LV-UEPI-N, Japan)

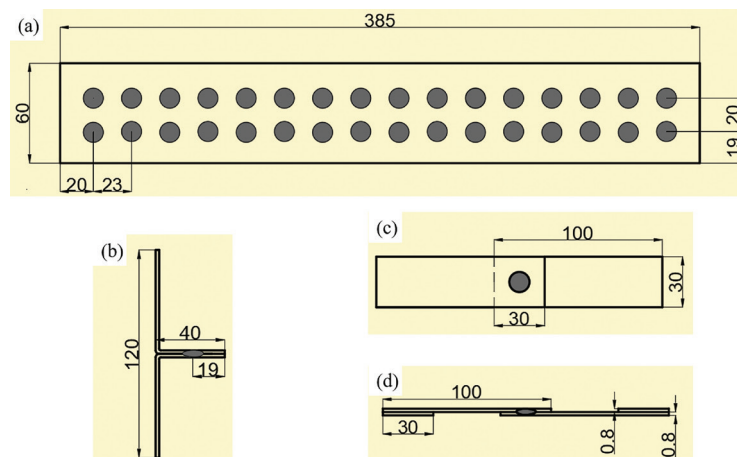


Figure 3: RSW workpieces specification and spot welding spacing (a) of large-sized galvanized steel sheets; (b) used in tearing tests; (c) used in shear tests; (d) used in tensile shear test.

after being treated according to the metallographic grinding and polishing procedures. The composition was detected by energy dispersive spectrometer (EDS) equipped with field emission scanning electron microscope (FE-SEM, Gemini SEM 300, Germany). The etching solution was configured according to the ratio of HCl (30ml): FeCl₃ (10g): deionized water (120ml). After the longitudinal section was etched for 15s, the metallographic structure was observed under a metallographic microscope. Then, 300ml of deionized water and 700ml of H₃PO₄ with a density of 1.71g/cm³ were added to form an electrolytic polishing solution, which was used to electropolishing the longitudinal sections at 1.5V for 10min. The microstructure was characterized by an electron backscatter diffraction (EBSD) detector mounted on the field emission scanning electron microscope.

The microhardness of the longitudinal sections of the failed electrodes was measured with an automatic microhardness tester (HMV-FA2, Japan) after the sample was subjected to metallographic grinding and polishing procedures. Measure once every 0.2mm between 0.2–3.8mm from the electrode tip, apply a load of 0.1N, and hold for 15s.

3. RESULTS AND ANALYSIS

3.1. Electrode life

Figure 4 shows that the nugget diameter and tensile shear limit load (TSFL) of the welds obtained by Cu@MWCNTs/Cu electrode and commercial CuCrZr electrode during RSW DP600 galvanized steel sheets change with the increase of the welds number. Here the horizontal dotted line represents the basis for judging electrode failure. The maximum nugget diameter obtained by CuCrZr electrode is 5.64mm at the 100th spot in Figure 4(a). The nugget diameter then drops sharply for every 100 welds until the 690th weld where the nugget diameter is less than the critical nugget size ($4\sqrt{\delta} = 3.8\text{mm}$), which is the basis for determining electrode failure based on the critical nugget size. Therefore, according to this criterion, it can be determined that the spot-welding life of CuCrZr electrode is 690 welds and the average diameter of effective welds (obtained before electrode failure) is 4.88mm. The maximum nugget diameter obtained by Cu@MWCNTs/Cu electrode is at the 500th weld, with a diameter of 5.96mm. Before 1000 welds, the nugget size decreases gently in a small fluctuation. Then the decreasing amplitude of the curve increases, until the 2150th weld, the nugget diameter decreases below the critical size. According to the same criteria, the spot-welding life of Cu@MWCNTs/Cu electrode under the experimental conditions was 2150 welds. The average diameter of effective welds is 5.17mm, which is slightly larger than that of CuCrZr electrode.

The TSFL of the 200th weld obtained by CuCrZr electrode reaches the maximum value of 6.13kN in Figure 4(b). Subsequently, the TSFL decreased sharply, which was similar to the nugget diameter curve. By 600 welds, it had dropped to less than 80% (4.84kN) of the 100th weld, which is the judgment basis of electrode failure based on TSFL. The average TSFL of effective welds (obtained before electrode failure) is 5.62kN. Therefore, according to this criterion, it can be determined that the life of CuCrZr electrode is 600 welds under the experimental conditions. The maximum TSFL value of Cu@MWCNTs/Cu electrode weld is located at the 500th weld, which is 6.59kN. The minimum value is 5.70kN at the 2200th weld. The TSFL curve fluctuates in these two value intervals and gradually decreasing, with an average TSFL of 6.02kN. However, when the electrode failure judgment based on the TSFL (TSFL is less than 80% (5.04kN) of the 100th weld), the 2200th

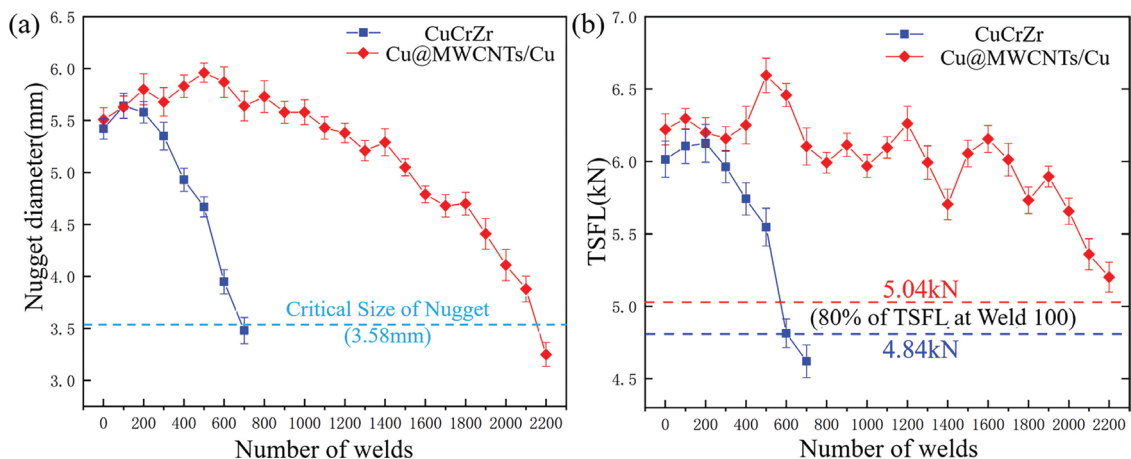
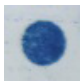



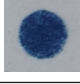
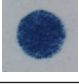
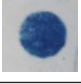

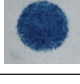
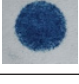
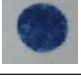

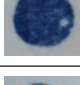
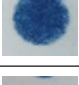
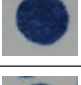

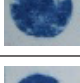
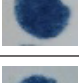
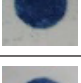
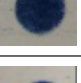
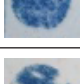
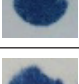
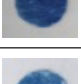
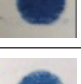
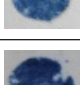
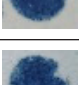
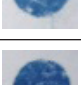
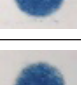



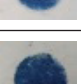
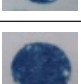






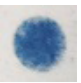
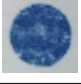

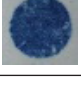

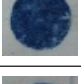
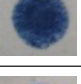






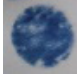


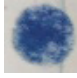
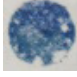
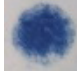
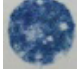





Figure 4: (a) Nugget diameter, (b) Tensile shear limit load (TSFL) versus number of welds for CuCrZr and Cu@MWCNTs/Cu electrodes.

Table 3: Carbon print photos of electrode tips.

NO. WELDS	CuCrZr		Cu@MWCNTs/Cu	
	UPPER	LOWER	UPPER	LOWER
1				
100				
200				
300				
400				
500				
600				
700				
800				
900				
1000				
1100				
1200				
1300				
1400				
1500				
1600				

(continued)

Table 3: (Continued)

NO. WELDS	CuCrZr		Cu@MWCNTs/Cu	
	UPPER	LOWER	UPPER	LOWER
1700				
1800				
1900				
2000				
2100				
2200				

weld of Cu@MWCNTs/Cu electrode (TSFL = 5.70kN>5.04kN) cannot be judged as failure. The overall bearing capacity of the welds obtained with Cu@MWCNTs/Cu electrode is significantly enhanced than that of CuCrZr electrode, which improves the reliability of the assembly connection.

Hence, in order to meet the above two electrode failure criteria, the life of CuCrZr electrode is 600 welds under the experimental conditions. The life of Cu@MWCNTs/Cu electrode is 2150 welds, which is more than 3 times the life of CuCrZr electrode.

3.2. Electrode tip morphology

Table 3 records the carbon imprinting on the end face of Cu@MWCNTs/Cu electrode and CuCrZr electrode during RSW DP600 galvanized steel sheets. Figure 5 shows the trend of the tip diameter of Cu@MWCNTs/Cu electrode and CuCrZr electrode with the increase of the welds, and the optical microscope photos of some representative electrode tips. It can be seen from Figure 5 that as the spot welding continues, the increase rate of the tip diameter of CuCrZr electrode presents three stages of ‘slow-fast-slow’ (regions: I, II, III), while the increase rate of the tip diameter of Cu@MWCNTs/Cu electrode presents three stages of ‘fast-slow-fast’ (regions: I, II, III). Overall, the tip diameter of CuCrZr electrode increased from 6mm to 8.53mm after 700 welds, while the tip diameter of Cu@MWCNTs/Cu electrode did not reach 8.46mm until 2000 welds. In short, plastic deformation occurred at the tips of both electrodes, and increased with the advancement of RSW DP600 galvanized steel sheets.

By comparing the representative optical microscope photos of the two material electrodes tips in the three regions in Figure 5, it can be found that there is no significant difference in the macroscopic morphology and size of the tip between Cu@MWCNTs/Cu electrode and CuCrZr electrode at the 50th weld (the initial stage of spot welding) in region I. The electrode tips remain smooth and flat, changing from bright purplish red to bleak silvery white, which is a typical copper-zinc color [13]. It shows that under the high temperature generated by spot welding resistance, the clamping force makes the electrode tips closely adhere to the surface of galvanized steel sheets, and the zinc coating reacts with Cu on the electrodes to form low melting point alloy layers. The darkened tip may be due to an oxidation reaction [14]. In region III, when Cu@MWCNTs/Cu electrode and CuCrZr electrode fail at the RSW end, the macroscopic morphology and size of the tips were also similar. The tip of the electrode becomes rough, the color was gray. And the periphery of the circle was burned black, all accompanied by an increase in area and pitting pits. In region II, it can be seen that CuCrZr electrode tip at the 300th weld began to appear irregularly shaped pitting pits, and a small amount of brass granular welds were distributed around the pits in the silvery white tip, as shown in Figure 5(c). Cu@MWCNTs/Cu electrode tip at the 1600th weld has irregularly shaped pitting pits, and the brassy granular welds are much larger than CuCrZr

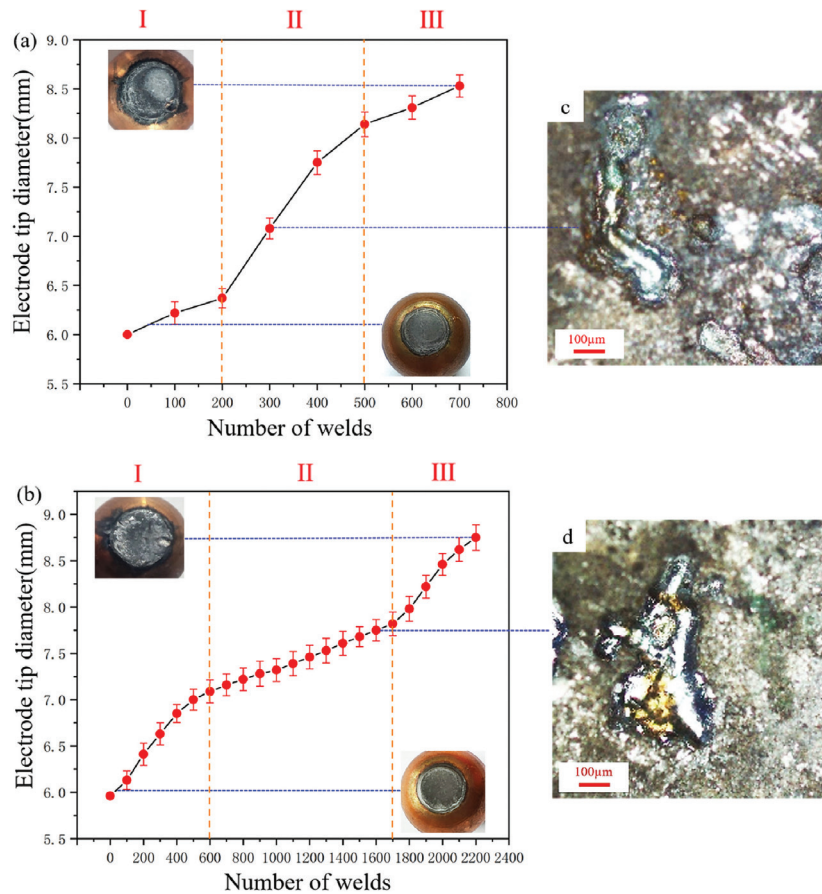


Figure 5: Tip diameter (a) CuCrZr and (b) Cu@MWCNTs/Cu electrodes versus number of welds.

electrode tip at the 300th weld, but not too severe, as shown in Figure 5(d). The formation of pitting corrosion pits may be due to the uneven distribution of the composition in the low melting point alloy layer of the electrode tips [15], which leads to the difference in thermal expansion performance in different parts of the layer. Under the high impact load and alternating temperature and stress caused by RSW, the alloy layer broke locally, adhered to the surface of galvanized steel sheets from the electrode tip, leaving pits on the electrode end face.

It can be determined referring to the optical microscope photos that the blank defect of the electrode tip imprinting in Table 3 is pitting pits. Pitting pits began to appear on CuCrZr electrode tip at about the 300th weld, and then pitting pits could be observed to grow and merge rapidly, and even develop into large cavities. Until the 600th weld, it was observed that some pitting pits began to become smaller and self-healing appeared. For Cu@MWCNTs/Cu electrode, the evolution process of tip pitting pits was similar, but the development process was much slower. Small pitting corrosion pits appeared until the 600th weld, and CuCrZr electrode was nearly ineffective in the same process. Until 1800 welds, the pitting pits on Cu@MWCNTs/Cu electrode tip became more and larger, and the pitting pits gradually became smaller (self-healing) at the 2100th weld.

It can be seen from the above that the degradation rate of CuCrZr electrode is much faster than that of Cu@MWCNTs/Cu electrode, whether it is the pitting pits or the tip diameter. For both electrodes, the development process of the tip pits changed almost synchronously with the rate of increase in the tip diameter, showing that the two were interrelated or affected. At the same time, both of them changed the effective working area of the electrode tips, thus changing the actual spot welding current density and current distribution, as well as the size and distribution of temperature and compressive stress at the electrode tips.

3.3. Microstructure, hardness and texture of longitudinal section of failed electrodes

Figure 6 shows the metallographic images of the longitudinal sections along the axis of the failed CuCrZr electrode and Cu@MWCNTs/Cu electrode. Figure 7 shows the hardness of the failed Cu@MWCNTs/Cu electrode and CuCrZr electrode at different depths from the end face. According to the characteristics of metallographies microstructure and microhardness, the longitudinal sections are divided into four regions I–IV along the depth. As shown in Figure 6, the transition between the microstructures of the four regions is gradient and gradual, so

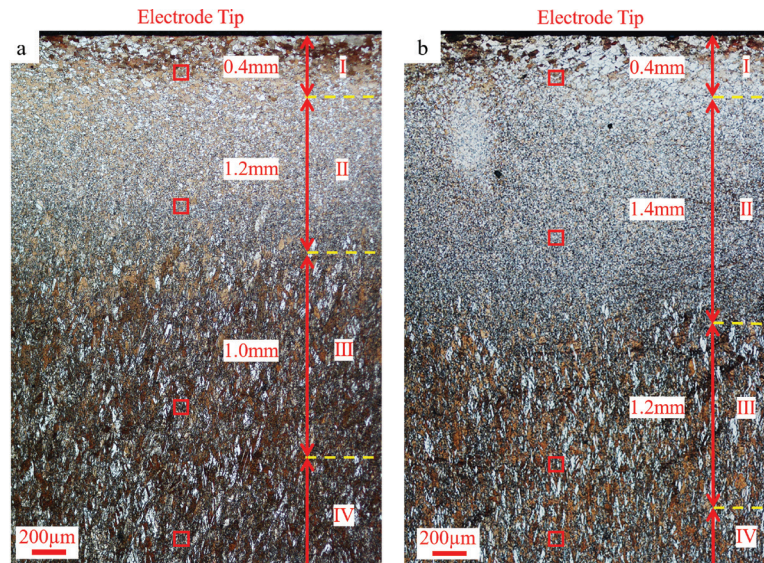


Figure 6: Metallographies microscope images of failed (a) CuCrZr electrode and (b) Cu@MWCNTs/Cu electrode at longitudinal sections along axis. The red box represents the location of the EBSD scan.

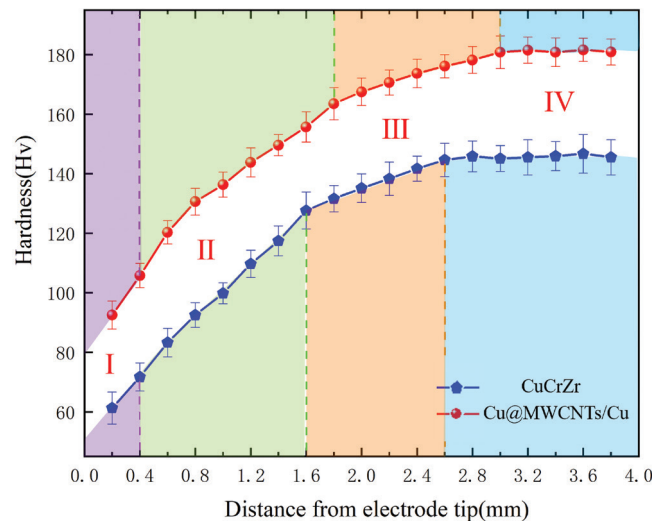


Figure 7: Hardness of failed CuCrZr electrode and Cu@MWCNTs/Cu electrode at different depths from the end face.

the boundary is undulating and blurred. The area depth value marked in Figure 6 is the median of the undulating boundary depth value. The two material electrodes are divided into four regions, the difference is that the depth range of the II and III regions of Cu@MWCNTs/Cu electrode is 0.2mm wider than that of CuCrZr electrode. This is because the spot welding life of CuCrZr electrode is 600 welds, and the RSW life of Cu@MWCNTs/Cu electrode is 2150 welds. The failed Cu@MWCNTs/Cu electrode has experienced about 2150 thermal RSW cycles, which is much more than about 600 thermal cycles of the failed CuCrZr electrode, resulting in the expansion of the heat affected zones.

The hardness of the two material electrodes in region I–III decreases with the decrease of the depth from the end face, and the decrease is close, as shown in Figure 7. However, the hardness of Cu@MWCNTs/Cu electrode in the four regions is 30–40Hv higher than that of CuCrZr electrode, which is due to the enhanced effect of the aligned MWCNTs in Cu matrix. During hardness testing, the load can be effectively transferred from Cu matrix to the stronger MWCNTs by the diamond indenter. MWCNTs bear a higher load than Cu matrix, resulting in an increase in the overall hardness of MWCNT/Cu composite. In addition, the amorphous transition zone at the MWCNTs/Cu interface stored dislocations and inhibits the movement of dislocations. The dislocation density increased, which increased the work hardening and further improved the hardness of the composites. For CuCrZr alloy electrodes, the coherent Cu₃Zr and pure Cr particles tend to age and formed incoherent particles at high temperatures [16], thereby reducing the mechanical properties of the material. During the continuous RSW cycle, the CuCrZr alloy was more prone to work hardening and recovery and recrystallization, so the electrode softened faster [17].

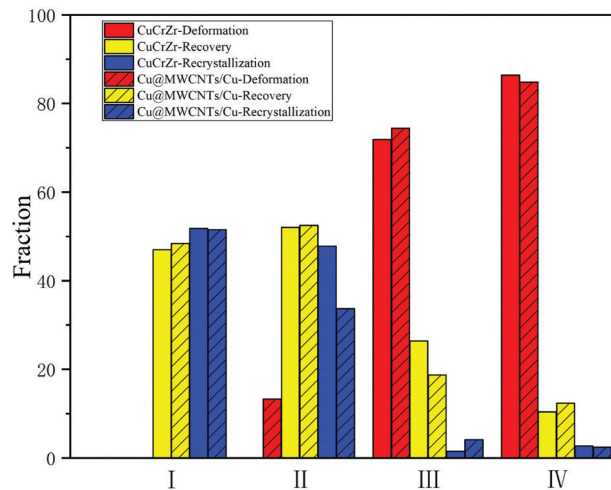


Figure 8: Content of deformed, recovered, and recrystallized grains in the red boxes in Figure 6 obtained by GOS analysis.

Region IV in Figure 6 is the substrate, the grain is slender, and the average grain size obtained by EBSD analysis is about $20.47\mu\text{m}$ (CuCrZr electrode) and $17.13\mu\text{m}$ (Cu@MWCNTs/Cu electrode). Among the four regions, region II is the easiest to identify, and its grains are dense, fine and white. The average grain sizes obtained by EBSD analysis are $6.84\mu\text{m}$ (CuCrZr electrode) and $5.05\mu\text{m}$ (Cu@MWCNTs/Cu electrode). As shown in Figure 7, the hardness of the two material electrodes in region II is much lower than that of the substrate (region IV). It shows that during the RSW cycle, region II experienced thermal histories above the recrystallization temperature (about 700°C) and recrystallized. The depth range of region I is about 0.4mm. The average grain size obtained by EBSD analysis is $12.09\mu\text{m}$ (CuCrZr electrode) and $7.39\mu\text{m}$ (Cu@MWCNTs/Cu electrode), which is much larger than that of region II. The hardness of the two material electrodes in region I is lower among the four regions, more than half lower than that of the substrate (region IV). It shows that during the RSW cycle in region I, the longest time or the highest temperature above the recrystallization temperature was enough to make the grain grow. As shown in Figure 6, there is no obvious difference between the microstructures in region III and IV, showing similar orientation texture. However, the hardness of the two material electrodes in region III is lower than that of the substrate (region IV), as shown in Figure 7. According to the distribution characteristics of the microhardness, the boundary between region III and region IV is divided. It shows that during the RSW cycle, region III experienced thermal histories above the recovery temperature (350°C), and a recovery occurred.

In fact, during the RSW cycle, the electrode tips were periodically subjected to impact loads such as current, resistance heat, pressure, and circulating water cooling. The micro-textures in different regions of the electrode tips evolve dynamically with the sharp increase and decrease of temperature and stress. When the electrode was not energized, but the load pressured, some areas may occurred work hardening; when the electrode was energized and the load pressure was simultaneously applied, the dynamic processed of work hardening, recovery and recrystallization occurred simultaneously in some areas. When the electrode was powered off and the pressure was unloaded, static recovery, static recrystallization and sub-dynamic recrystallization occurred simultaneously in some areas still at high temperature. Because the resistance heat was transmitted from the electrode tip into its inside, the circulating water cooling in the electrode continuously took away the heat. Therefore, dynamic recovery and recrystallization did not occur immediately from the beginning of RSW, but work hardening and recovery first with the increase of temperature. Only when the local temperature rose to the recrystallization temperature and the deformation reached a certain degree, recrystallization occurred, which was a process that accumulates slowly with the time line. Thus, four regions were formed along the electrode depth as shown in Figure 7, that is, region I (grain growth), region II (recrystallization), region III (recovery), and region IV (substrate). To further understand the macrottextures of the two material electrodes after failure, the red box positions are selected in the four regions shown in Figure 6 for EBSD analysis. Figure 8 shows the content of deformed, recovered, and recrystallized grains in the red box in Figure 6 obtained by grain orientation diffusion (GOS) analysis. Here the grains with GOS of $0^\circ\text{--}2^\circ$ are determined as recrystallized grains, the grains with GOS of $2^\circ\text{--}7^\circ$ are determined as recovery grains, and the grains with GOS greater than 7° are deformed grains [18–20]. It is worth noting that the EBSD results gradually change with the sampling depth, and the content of the above three types of grains also gradually changes.

Figure 9 shows the electron backscatter diffraction (EBSD) data corresponding to the red boxes of the failed CuCrZr electrode and Cu@MWCNTs/Cu electrode in region IV (substrate) in Figure 6, including the

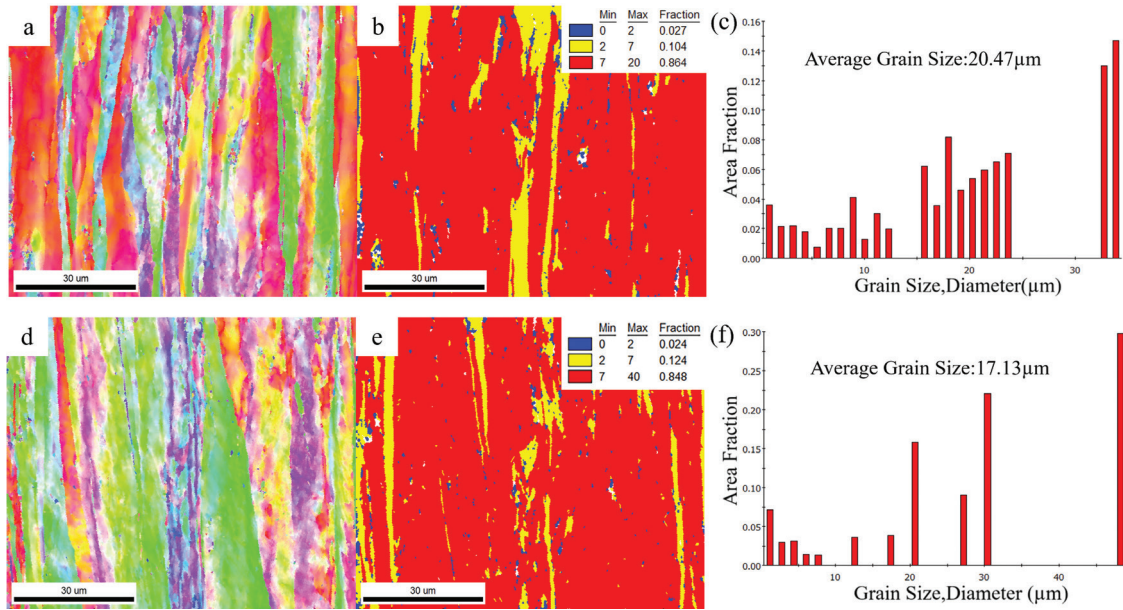


Figure 9: EBSD data corresponding to the red box in region IV in Figure 6: Longitudinal profile of failed CuCrZr electrode: (a) IPF diagram, (b) GOS diagram, (c) grain size distribution; failed Cu@MWCNTs/Cu electrode: (d) IPF diagram, (e) GOS diagram, (f) grain size distribution.

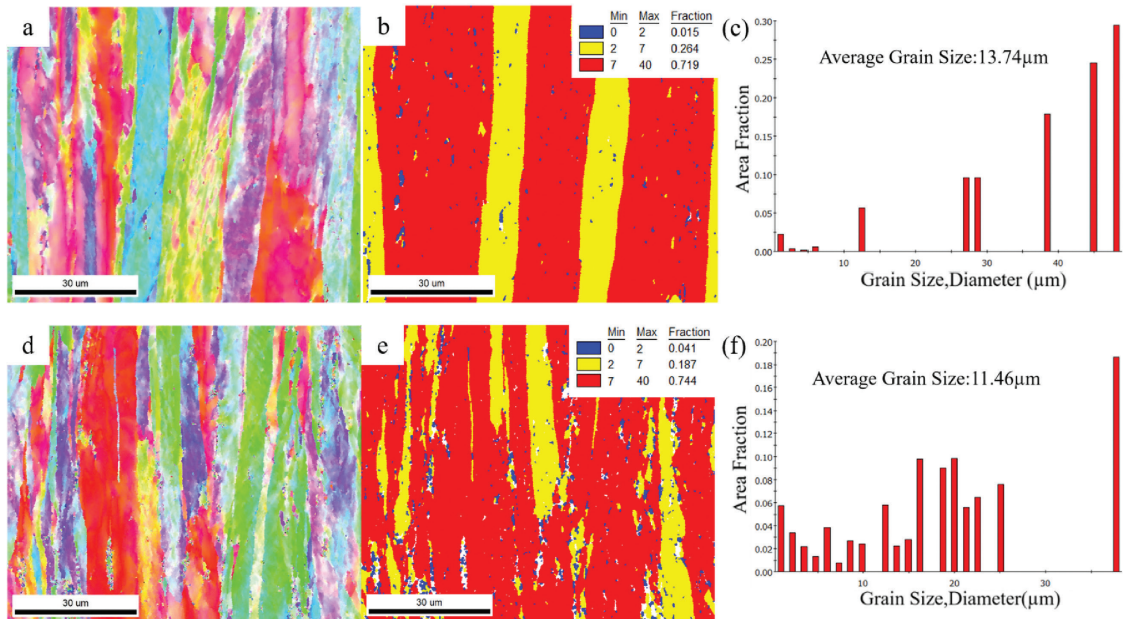


Figure 10: EBSD data corresponding to the red box in region III in Figure 6: Longitudinal profile of failed CuCrZr electrode: (a) IPF diagram, (b) GOS diagram, (c) grain size distribution; failed Cu@MWCNTs/Cu electrode: (d) IPF diagram, (e) GOS diagram, (f) grain size distribution.

inverse pole figure (IPF), GOS diagram and grain size distribution. As shown in Figure 9(a) and 9(d) IPF diagrams, the grains of the two material electrodes in region IV show obvious fiber orientation texture along the axial direction $\langle 100 \rangle$ and $\langle 111 \rangle$, which is due to the cold working deformation of the electrode such as hot extrusion followed by cold drawing treatment elongated grains. It can be seen from Figure 8, Figure 9(b) and 9(e) that the proportion of grains in region IV of the two materials electrodes is close, but the proportion of deformed grains and recrystallized grains in CuCrZr electrode is slightly higher than that of Cu@MWCNTs/Cu electrode. The recovery grains are less.

Figure 10 shows the EBSD data corresponding to the failed CuCrZr electrode and Cu@MWCNTs/Cu electrode in the red box of region III (recovery) in Figure 6. As shown in Figure 10(a) and 10(d) IPF, the orientation textures of the two material electrodes are similar to those of the IV region substrate. From Figure 8,

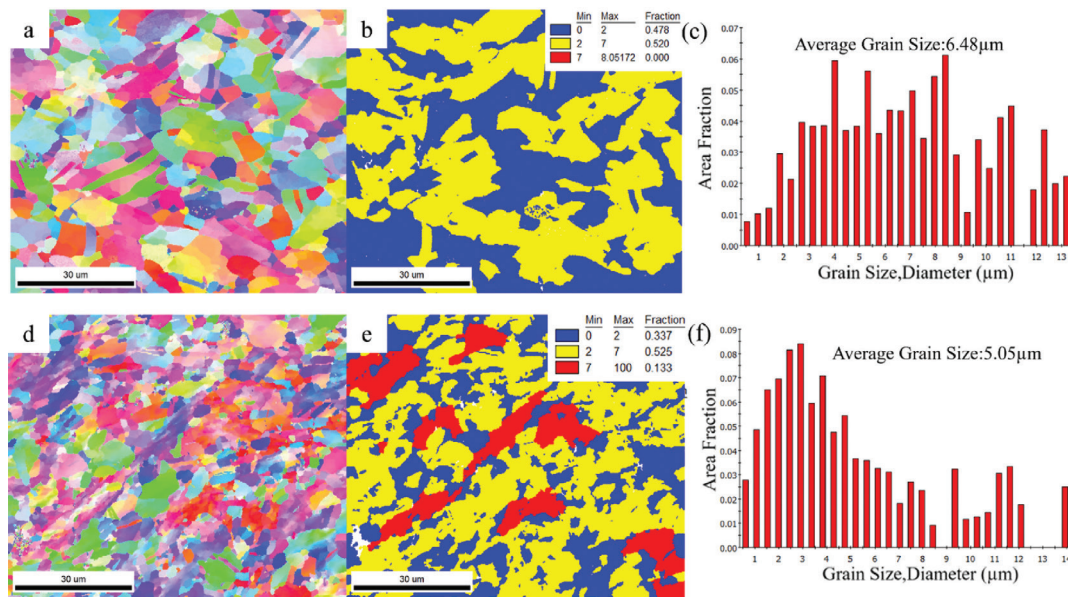


Figure 11: EBSD data corresponding to the red box in region II in Figure 6: Longitudinal profile of failed CuCrZr electrode: (a) IPF diagram, (b) GOS diagram, (c) grain size distribution; failed Cu@MWCNTs/Cu electrode: (d) IPF diagram, (e) GOS diagram, (f) grain size distribution.

Figure 10(b) and 10(e), it can be seen that compared with region IV, the recovery grains of the two material electrodes in region III increased by more than 10%, while the deformed grains decreased by more than 10%, and the recrystallized grains did not change much. In addition, Cu@MWCNTs/Cu electrode has less recovery grains in the III regions than CuCrZr electrode. This may be due to the enhanced phase MWCNTs with excellent axial thermal conductivity can conduct the resistance heat generated by RSW away faster, and the residence time of region III of Cu@MWCNTs/Cu composite electrode at recovery temperature is shorter than that of CuCrZr alloy electrode. Copper this face-centered cubic lattice of metal stacking fault energy is low, and the region III far away from the electrode tip, RSW cycle, temperature and stress is relatively low, so the degree of thermo-plastic deformation is small, low dislocation density, work hardening and recovery.

Figure 11 shows the EBSD data corresponding to the failed CuCrZr electrode and Cu@MWCNTs/Cu electrode in the red box of region II (recrystallization), as shown in Figure 6. As shown in Figure 11(a) and 11(d) IPF, compared with the orientation texture of region IV substrate, the grains of the two material electrodes in region II are equiaxed, and the grain size is about 2 times smaller than that of region IV substrate. It can be seen from Figure 8, Figure 11(b) and 11(e) that the recovery grains and recrystallized grains of the two material electrodes in region II are greatly increased compared with region III. Especially for recrystallized grains, CuCrZr electrode increased from 1.5% in region III to 47.8% in region II. Cu@MWCNTs/Cu electrode increased from 4.1% in region III to 33.7% in region II. region II is close to the electrode tip, and the temperature and stress are higher than region III during the RSW cycle, often above the recrystallization temperature. The time for resistance heat to be generated by one cycle of spot welding is very short (only 0.2s), and recrystallization requires a certain incubation time above the recrystallization temperature, which suspends recrystallization in a single cycle. In the subsequent spot welding cycle, when the temperature exceeds the recrystallization temperature, the dynamic recrystallization nuclei that have not yet grown and the recrystallization grains that have stopped will continue to grow. This sub-dynamic recrystallization process is very rapid because it does not require nucleation time and incubation period. The region II is in the dynamic softening process of hardening, recovery and recrystallization, and the work hardening is offset by recovery and recrystallization at any time, and finally most of the microstructure evolves into recrystallization microstructure.

In addition, the content of recrystallized grains in region II of Cu@MWCNTs/Cu electrode is less than that of CuCrZr electrode. Considering that the failed Cu@MWCNTs/Cu electrode has experienced about 2150 spot welding thermal cycles, which is much more than about 600 thermal cycles of the failed CuCrZr electrode, the dynamic recrystallization process is much slower. This is partly due to the pinning effect of MWCNTs, on the other hand, due to the excellent axial thermal conductivity of Cu@MWCNTs/Cu composites, the resistance heat generated by RSW can be guided away faster, and the residence time of Cu@MWCNTs/Cu electrode region II at recrystallization temperature is shorter than that of CuCrZr alloy electrode, which can slow down or curb the dynamic recrystallization process in time.

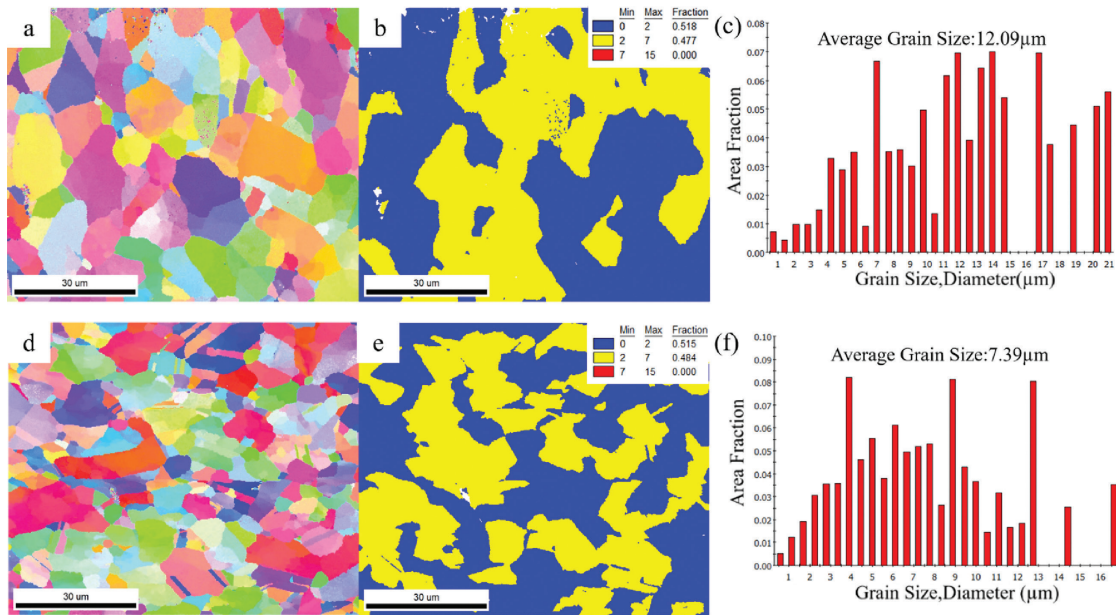


Figure 12: EBSD data corresponding to the red box in region I in Figure 6: Longitudinal profile of failed CuCrZr electrode: (a) IPF diagram, (b) GOS diagram, (c) grain size distribution; failed Cu@MWCNTs/Cu electrode: (d) IPF diagram, (e) GOS diagram, (f) grain size distribution.

Figure 12 shows the EBSD data corresponding to the red box of the failed CuCrZr electrode and Cu@MWCNTs/Cu electrode in region I (grain growth), as shown in Figure 6. The grains of the two material electrodes in region I still maintain a similar equiaxed shape in region II, but the grain size is about twice that of the substrate in region II, As shown in Figure 12(a) and 12(d) IPF. The region II is located at the electrode tip, which is the highest temperature and stress position during the RSW cycle, and the recrystallization temperature was first reached to start recrystallization. region II also lasts for the longest time above the recrystallization temperature, resulting in grain growth, deterioration of mechanical properties and obvious decrease of plasticity. When the electrode pressure and high temperature were coupled, plastic deformation occurs at the softened electrode end, which was gradually squeezed outward extension, and finally developed into a ‘mushroom shape’, as shown in Figure 13. The ‘mushroom-like’ deformation of the Cu@MWCNTs/Cu electrode tip in Figure 13 is significantly smaller than that of CuCrZr electrode. This may be due to the reinforcements MWCNTs with excellent high temperature mechanical properties significantly increases the deformation activation energy of Cu@MWCNTs/Cu composite at high temperatures, thereby enhancing the thermal deformation resistance of Cu@MWCNTs/Cu electrode [21] and slowing down its plastic deformation.

However, the grain size of Cu@MWCNTs/Cu electrode in region II is about 26% smaller than that of CuCrZr electrode. This may be due to the fact that MWCNTs, as a source of subgrain boundary nucleation, can also effectively prevent the grain growth of the Cu matrix in the middle and late stages of the spot-welding process through the pinning effect [22], thus acting as a grain refinement in Cu@MWCNTs/Cu composites [23].

3.4. Microstructure and composition of surface profile of failure electrode

Figure 14(a) and 14(b) show the optical microscopy images of the longitudinal sections along the axis of the failed CuCrZr electrode and Cu@MWCNTs/Cu electrode tips. It can be seen that the surface of the two materials electrode tips is divided into different color layers, which are marked with red dotted lines. Among them, CuCrZr electrode tips has five layers, which are different from the substrate color, and the total thickness is about 45 μm; Cu@MWCNTs/Cu tips has three layers, which are different from the substrate color, with a total thickness of about 22 μm. From the EDS spectra shown in Figure 14(c) and 14(d), it can be seen that O, Fe and Zn are distributed along the longitudinal section of the failed (c) CuCrZr electrode and (d) Cu@MWCNTs/Cu electrode surface, and the proportion of Cu element is significantly smaller than that of the substrate. The Cu element on the two materials electrodes tips showed a ‘gear’ distribution, but the distribution boundary of Cu@MWCNTs/Cu electrode is smoother.

The XRD results of the longitudinal section along the axis of the failed Cu@MWCNTs/Cu electrode and CuCrZr electrode tips in Figure 14(e) show that the peak strength of Fe₄Zn₉ on the Cu@MWCNTs/Cu electrode tip is higher than that of CuCrZr electrode, indicating that the content of Fe₄Zn₉ phase is more and the grain size

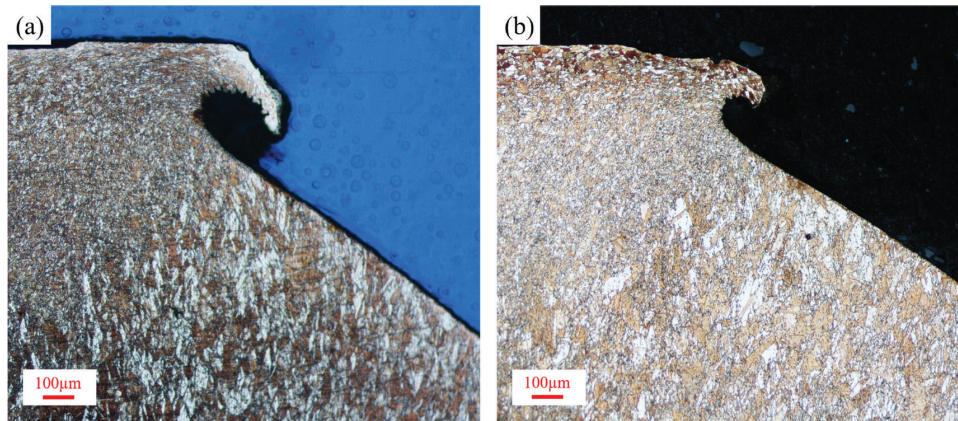


Figure 13: SEM images of failed (a) CuCrZr electrode and (b) Cu@MWCNTs/Cu electrode tip.

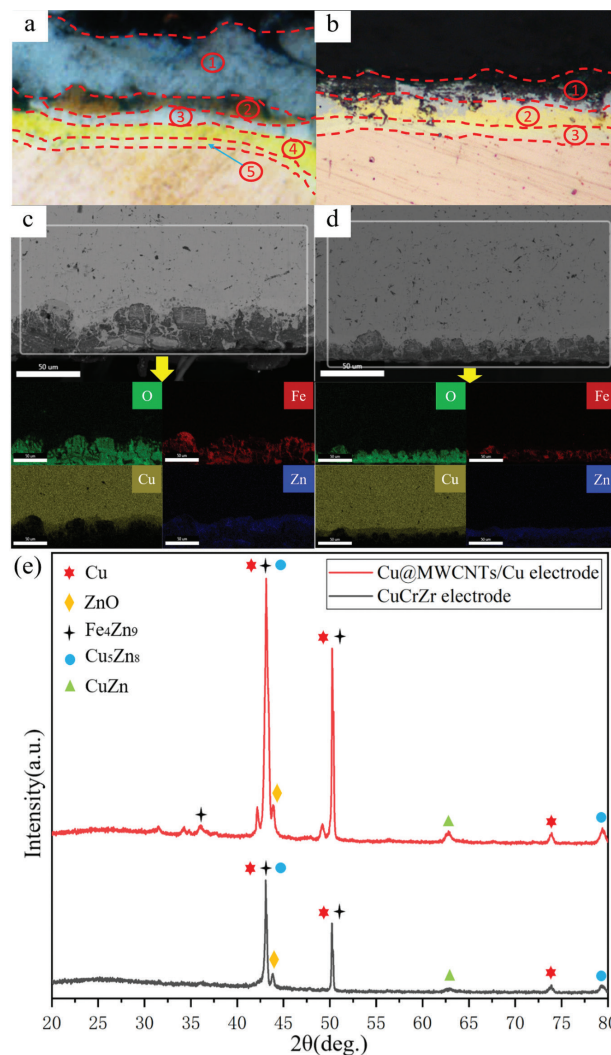


Figure 14: SEM images,EDS patterns and (e) XRD patterns of longitudinal section along axis of failed (a,c) CuCrZr electrode and (b,d) Cu@MWCNTs/Cu electrode surface.

is larger. It is precisely because this iron-rich layer delays or prevents the penetration of Zn into the electrode matrix during electrode operation[24] that the alloy layer of Cu@MWCNTs/Cu electrode was thinner than the CuCrZr electrode.

Based on the above information, the five layers of CuCrZr electrode in Figure 14(a) are: the first layer and the second layer are porous iron-zinc phase and oxide, the third layer is white γ -brass phase, the fourth layer

is yellow β -brass phase, and the fifth layer is yellow α -brass phase. And the three layers of Cu@MWCNTs/Cu electrode tip in Figure 14(b): the first layer is iron-rich iron-zinc phase and oxide, the second layer and the third layer are brass phase composed of β -copper zinc and α -copper zinc, respectively.

The hard and brittle γ -brass phase formed at the electrode end, which was easy to crack and fall off under the action of welding force, thus causing pitting corrosion at the electrode tip during RSW galvanized steel sheet [25]. MWCNTs in Cu@MWCNTs/Cu electrode play a pinning effect, which can maintain higher mechanical properties and toughness. At the same time, compared with CuCrZr electrode, the Zn content in the alloy layer of Cu@MWCNTs/Cu electrode is lower. Cu@MWCNTs/Cu electrode was infiltrated by Zn more shallowly, and the alloy layer at the tip was thinner than that of CuCrZr electrode during RSW. Therefore, Cu@MWCNTs/Cu electrode has a stronger ability to resist cracking and pitting, which effectively slows down the failure rate of the electrode and makes the spot welding life of Cu@MWCNTs/Cu electrode longer.

4. CONCLUSION

This work evaluated the life of Cu@MWCNTs/Cu composite electrode RSW galvanized steel sheets. MWCNTs are arranged in the electrode along the conduction direction of RSW working electricity and force. The macro/micro morphology, microstructure characteristics and defects, hardness, texture and composition of the failed electrode were studied, and compared with the commercially available CuCrZr electrode. The related mechanism of spot welding performance enhancement and failure of composite electrode was revealed.

1. The RSW life of Cu@MWCNTs/Cu electrode (2150 welds) is 3 times longer than that of CuCrZr electrode (600 welds), and the degradation rate is much slower. This is attributed to the fact that MWCNTs are arranged in a straight and long state along the working electrical/force conduction direction, which improves the conductivity, mechanical properties and thermal deformation resistance of Cu@MWCNTs/Cu electrode.
2. The hardness of Cu@MWCNTs/Cu electrode is 30–40Hv higher than that of CuCrZr electrode. This is mainly due to the strengthening effect of oriented MWCNTs on the composites and the inhibition of dislocation motion by the amorphous transition region at the MWCNTs/Cu interface.
3. The longitudinal cross-sections of the failed two material electrodes show four regions, region I (grain growth), region II (recrystallization), region III (recovery) and region IV (substrate). The grains of the two material electrodes in region I and region II are equiaxed, and the grains in region III and region IV are fiber-oriented texture. The content of recrystallization grains in region II and recovery grains in region III of Cu@MWCNTs/Cu electrode is less than that of CuCrZr electrode. This is partly due to the pinning effect of MWCNTs. On the other hand, MWCNTs with excellent axial thermal conductivity can export RSW heat faster. The residence time of Cu@MWCNTs/Cu electrode at high temperature was shorter than that of CuCrZr alloy electrode, which slows down or curbs the dynamic recrystallization/recovery process in time.
4. There are 5 layers of alloy in CuCrZr electrode tip: iron-zinc phase and oxide, γ -brass phase, β -brass phase, α -brass phase. Cu@MWCNTs/Cu electrode tip has three layers of alloy: iron-rich iron-zinc phase and brass phase composed of oxide, β -copper-zinc and α -copper-zinc. Due to the pinning effect of MWCNTs, Cu@MWCNTs/Cu electrode has higher mechanical properties and toughness. At the same time, the Zn content in Cu@MWCNTs/Cu electrode tip is lower than that of CuCrZr electrode, and its alloy layer is thinner. Therefore, Cu@MWCNTs/Cu electrode has a stronger ability to resist cracking and pitting, which effectively slows down the failure rate of the electrode and makes RSW life of Cu@MWCNTs/Cu electrode longer.

5. ACKNOWLEDGMENTS

This work was supported by the National Natural Science Foundation of China (Nos.51775176).

6. BIBLIOGRAPHY

- [1] ERTEK EMRE, H., BOZKURT, B., “Effect of Cr-Ni Coated Cu-Cr-Zr electrodes on the mechanical properties and failure modes of TRIP800 spot weldments”, *Engineering Failure Analysis*, v. 110, pp. 104439, 2020. doi: <http://dx.doi.org/10.1016/j.engfailanal.2020.104439>.
- [2] MALMIR, M., SHEIKHI, M., MAZAHARI, Y., *et al.*, “Substantial electrode life enhancement in resistance spot welding of galvanized steels through nanolayered multi-layer CrN/(Cr,Al)N coating”, *Surface Engineering*, v. 37, n. 9, pp. 1163–1175, 2021. doi: <http://dx.doi.org/10.1080/02670844.2021.1951512>.
- [3] CHEN, T., LING, Z., WANG, M., *et al.*, “Effect of a slightly concave electrode on resistance spot welding of Q&P1180 steel”, *Journal of Materials Processing Technology*, v. 285, pp. 116797, 2020. doi: <http://dx.doi.org/10.1016/j.jmatprotec.2020.116797>.

- [4] ZHAO, D., REN, D., SONG, G., *et al.*, “Comparison of mechanical properties and the nugget formation of composite ceramic-centered annular welding and traditional resistance spot welding”, *International Journal of Mechanical Sciences*, v. 187, pp. 105933, 2020. doi: <http://dx.doi.org/10.1016/j.ijmecsci.2020.105933>.
- [5] LI, M., WANG, Y., YANG, S., *et al.*, “Improving mechanical properties and electrode life for joining aluminum alloys with innovatively designated newton ring electrode”, *Journal of Manufacturing Processes*, v. 64, pp. 948–959, 2021. doi: <http://dx.doi.org/10.1016/j.jmapro.2021.02.001>.
- [6] WU, Z., SHAN, P., LIAN, J., *et al.*, “Effect of deep cryogenic treatment on electrode life and microstructure for spot welding hot dip galvanized steel”, *Materials & Design*, v. 24, n. 8, pp. 687–692, 2003. doi: [http://dx.doi.org/10.1016/S0261-3069\(03\)00029-3](http://dx.doi.org/10.1016/S0261-3069(03)00029-3).
- [7] ZHENG, Z., YANG, A., TAO, J., *et al.*, “Mechanical and conductive properties of Cu matrix composites reinforced by oriented carbon nanotubes with different coatings”, *Nanomaterials (Basel, Switzerland)*, v. 12, n. 2, pp. 266, 2022. doi: <http://dx.doi.org/10.3390/nano12020266>. PubMed PMID: 35055283.
- [8] ZHENG, Z., CHEN, Y., ZHANG, M., *et al.*, “Fabrication of CNTs/Cu composites with orthotropic mechanical and tribological properties”, *Materials Science and Engineering A*, v. 804, pp. 140788, 2021. doi: <http://dx.doi.org/10.1016/j.msea.2021.140788>.
- [9] RADHAMANI, A.V., LAU, H.C., RAMAKRISHNA, S., “CNT-reinforced metal and steel nanocomposites: a comprehensive assessment of progress and future directions”, *Composites. Part A, Applied Science and Manufacturing*, v. 114, pp. 170–187, 2018. doi: <http://dx.doi.org/10.1016/j.compositesa.2018.08.010>.
- [10] SAMANI, M.K., KHOSRAVIAN, N., CHEN, G.C.K., *et al.*, “Thermal conductivity of individual multiwalled carbon nanotubes”, *International Journal of Thermal Sciences*, v. 62, pp. 40–43, 2012. doi: <http://dx.doi.org/10.1016/j.ijthermalsci.2012.03.003>.
- [11] EBBESEN, T.W., LEZEC, H.J., HIURA, H., *et al.*, “Electrical conductivity of individual carbon nanotubes”, *Nature*, v. 382, n. 6586, pp. 54–56, 1996. doi: <http://dx.doi.org/10.1038/382054a0>.
- [12] ZHENG, Z., LIU, J., TAO, J., *et al.*, “Effect of electroless coatings on mechanical properties and wear behavior of oriented multiwall carbon nanotubes reinforced copper matrix composites”, *Nanomaterials (Basel, Switzerland)*, v. 11, n. 11, pp. 2982, 2021. doi: <http://dx.doi.org/10.3390/nano11112982>. PubMed PMID: 34835746.
- [13] GALLAGHER, M., “*Electrode wear in the resistance spot welding of galvanized steel sheet*”, D.Sc. Thesis, University of Windsor, Canada, 2003.
- [14] MAHMUD, K., MURUGAN, S.P., CHO, Y., *et al.*, “Geometrical degradation of electrode and liquid metal embrittlement cracking in resistance spot welding”, *Journal of Manufacturing Processes*, v. 61, pp. 334–348, 2021. doi: <http://dx.doi.org/10.1016/j.jmapro.2020.11.025>.
- [15] ZHANG, X.Q., CHEN, G.L., ZHANG, Y.S., “Characteristics of electrode wear in resistance spot welding dual-phase steels”, *Materials & Design*, v. 29, n. 1, pp. 279–283, 2008. doi: <http://dx.doi.org/10.1016/j.matdes.2006.10.025>.
- [16] PARKER, J.D., WILLIAMS, N.T., HOLLIDAY, R.J. “Mechanisms of electrode degradation when spot welding coated steels”, *Science and Technology of Welding and Joining*, v. 3, n. 2, pp. 65–74, 1998. doi: <http://dx.doi.org/10.1179/stw.1998.3.2.65>.
- [17] LUO, P., DONG, S.J., SUN, S.X., *et al.*, “Electrospark deposition of ZrB₂-TiB₂ composite coating on Cu-Cr-Zr alloy electrodes”, *Surface Science and Engineering*, v. 10, n. 1, pp. 54, 2016. doi: <http://dx.doi.org/10.1504/ijsurfse.2016.075316>.
- [18] FIELD, D., BRADFORD, L., NOWELL, M., *et al.*, “The role of annealing twins during recrystallization of Cu”, *Acta Materialia*, v. 55, n. 12, pp. 4233–4241, 2007. doi: <http://dx.doi.org/10.1016/j.actamat.2007.03.021>.
- [19] KONKOVA, T., MIRONOV, S., KORZNIKOV, A., *et al.*, “On the room-temperature annealing of cryogenically rolled copper”, *Materials Science and Engineering A*, v. 528, n. 24, pp. 7432–7443, 2011. doi: <http://dx.doi.org/10.1016/j.msea.2011.06.047>.
- [20] HARSHAVARDHANA, N., SIVAM, S.P.S.S., KUMAR, G., *et al.*, “A comparative study on misorientations to determine the extent of recrystallization in pure ETP copper”, *The Physics of Metals and Metallography*, v. 122, n. 13, pp. 1279–1287, 2021. doi: <http://dx.doi.org/10.1134/S0031918X20140094>.
- [21] LIU, J., FAN, G., TAN, Z., *et al.*, “Mechanical properties and failure mechanisms at high temperature in carbon nanotube reinforced copper matrix nanolaminated composite”, *Composites. Part A, Applied Science and Manufacturing*, v. 116, pp. 54–61, 2019. doi: <http://dx.doi.org/10.1016/j.compositesa.2018.10.022>.

- [22] HU, T., MA, K., TOPPING, T.D., *et al.*, “Improving the tensile ductility and uniform elongation of high-strength ultrafine-grained Al alloys by lowering the grain boundary misorientation angle”, *Scripta Materialia*, v. 78–79, pp. 25–28, 2014. doi: <http://dx.doi.org/10.1016/j.scriptamat.2014.01.020>.
- [23] WANG, H., ZHANG, Z., HU, Z., *et al.*, “Improvement of interfacial interaction and mechanical properties in copper matrix composites reinforced with copper coated carbon nanotubes”, *Materials Science and Engineering A*, v. 715, pp. 163–173, 2018. doi: <http://dx.doi.org/10.1016/j.msea.2018.01.005>.
- [24] XING, B.B., YAN, S.H., ZHOU, H.Y., *et al.*, “Qualitative and quantitative analysis of misaligned electrode degradation when welding galvanized steel”, *International Journal of Advanced Manufacturing Technology*, v. 97, n. 1–4, pp. 629–640, 2018. doi: <http://dx.doi.org/10.1007/s00170-018-1958-1>.
- [25] LUO, P., XIONG, C., WANG, C., *et al.*, “Comparative failure analysis of electrodes coated with TiB₂-ZrB₂ and TiB₂-ZrB₂/Ni layers”, *Surface and Coatings Technology*, v. 317, pp. 83–94, 2017. doi: <http://dx.doi.org/10.1016/j.surfcoat.2017.03.045>.